values of the quadrupole splittings over the wide range of temperature up to 600 °K. In our calculation of energy splittings and quadrupole splittings we have neglected covalency effects.[8] The direction cosines of the principal axes, x', y', and z' of the electric-field-gradient tensor at 4 °K are calculated to be x' axis (0, 0, 1), y' axis (-0.03682 ± 0.00007, 0.99932 ± 0.00001, 0), and z' axis (0.99932 ± 0.00001, 0.03682 ± 0.00007, 0). This means that the direction of the maximum electric field gradient is nearly parallel to the b_0 axis within $(2.12 \pm 0.01)°$, which is consistent with neutron-diffraction measurements[2] and Mössbauer measurements[3] at liquid-helium temperature.

†Work supported by the Ministry of Science and Technology, Republic of Korea.

[1]R. W. G. Wyckoff, *Crystal Structures* (Wiley-Interscience, New York, 1964), Vol. III.
[2]B. C. Frazer and P. J. Brown, Phys. Rev. 125, 1283 (1962).
[3]K. Ono and A. Ito, J. Phys. Soc. Japan 19, 899 (1964).
[4]R. Ingalls, Phys. Rev. 133, A787 (1964).
[5]Hang Nam Ok, Kyun Nahm, and Soo Wan Lee, New Phys. (Korea) 10, 117 (1970).
[6]Hang Nam Ok, Phys. Rev. 185, 477 (1969).
[7]L. Pauling, *The Nature of the Chemical Bond* (Cornell U. P., Ithaca, New York, 1960), p. 321.
[8]A. J. Nozik and M. Kaplan, Phys. Rev. 159, 273 (1967).
[9]A. J. Freeman and R. E. Watson, Phys. Rev. 131, 2566 (1963).
[10]R. E. Trees, Phys. Rev. 82, 683 (1951).

PHYSICAL REVIEW B VOLUME 4, NUMBER 11 1 DECEMBER 1971

Ultrasonic Attenuation and Mn^{55} Nuclear Acoustic Resonance in MnTe

K. Walther
Philips Forschungslaboratorium Hamburg GmbH, Hamburg 54, *Germany*
(Received 24 February 1970; revised manuscript received 17 May 1971)

The ultrasonic attenuation in MnTe for longitudinal waves with propagation vector in the hexagonal plane was measured as a function of temperature for frequencies up to 530 MHz. The attenuation below the Néel temperature comprises both background losses and an extraordinarily intense (attenuation up to 300 dB/cm) temperature-dependent resonance absorption caused by Mn^{55} nuclear acoustic resonance. Extrapolation to zero temperature yields a resonance frequency $f_{NAR} = 466.5$ MHz and a hyperfine field $H_n = 442$ kOe. Theoretical expressions for the sound absorption due to electronic and nuclear spins were derived. Comparison with the measured magnetic-field dependence of background and nuclear-acoustic-resonance (NAR) absorption suggests that spins located in domains rather than inside domain walls are mainly responsible for the observed effects. The spin-flop fields, observed in the NAR experiments, are much higher than the values calculated from anisotropy constants and susceptibilities. Good agreement between experiments and theory is obtained for $H \gg H_{SF}$.

I. INTRODUCTION

Nuclear-magnetic-resonance studies in antiferromagnetic materials provide detailed information about the magnetic ordering, since nuclei in these substances experience a strong hyperfine field H_n proportional to the electronic sublattice magnetization M. The corresponding nuclear resonances occur in the frequency range of several hundred MHz and can be excited both with rf magnetic fields (NMR)[1] and ultrasonic waves [nuclear acoustic resonance (NAR)].[2-4]

An extraordinarily intense ultrasonic resonance absorption in the antiferromagnetic semiconductor MnTe was observed by the author[3] and interpreted as being due to NAR of the Mn^{55} nucleus. Strength and magnetic-field dependence of the resonance were explained previously[3] in terms of the driving field enhancement mechanism occurring within domain walls.[5] In this paper we present a more detailed account on the Mn^{55} NAR in MnTe, demonstrating that spins located in domains are mainly responsible for the observed effects, contrary to the previous interpretation.[3]

The antiferromagnetic modification of MnTe crystallizes in the NiAs structure,[6] in which the magnetic cations form a simple hexagonal lattice. The Néel temperature, below which antiferromagnetic ordering occurs, is $T_N = 306.7$ °K.[3,7-9] In the antiferromagnetic phase the average spin directions in each plane perpendicular to the hexagonal axis (c plane) are parallel to each other and antiparallel to those of the Mn atoms in the adjacent c plane.[10-12] A strong anisotropy force causes the spin directions to be oriented perpendicular to the c axis. MnTe is thus an "easy-plane" antiferromagnet with

two antiparallel sublattices of electronic magnetization. A weak anisotropy force of sixfold symmetry occurs in the c plane.[10]

When oscillations of the electronic sublattice magnetization are excited far below the antiferromagnetic-resonance (AFMR) frequencies, the largest excursions occur for the mode with motion predominantly in the c plane. This mode can be excited magneto-elastically using either longitudinal ultrasonic waves with a propagation vector $\vec{q}$ in the c plane or for the xy shear wave with both propagation and polarization vectors located in the c plane. The nuclear spin systems are excited via the hyperfine interaction.

In this paper we first discuss (Sec. II B) measurements of the ultrasonic attenuation for longitudinal waves in MnTe. Three different loss mechanisms are observed: (i) "critical" scattering at the Néel temperature T_N, (ii) nonresonant background absorption, and (iii) Mn^{55} NAR absorption. Experimental results on the magnetic-field dependence of background and NAR absorption are reported in Sec. II C. Theoretical expressions for the acoustic absorption coefficients due to electronic and nuclear spins in domains and inside domain walls are derived in Sec. III. The experimental results are compared with theoretical predictions in Sec. IV. The measured field dependence of the NAR absorption suggests that spins located in domains rather than inside walls are mainly responsible for the observed effects. Good agreement with theory is obtained for magnetic fields H, large compared with the spin-flop field H_{SF}, whereas the observed behavior for small magnetic fields is complicated and cannot yet be interpreted quantitatively.

II. EXPERIMENTS

A. Experimental Procedure

Ultrasonic transmission experiments were carried out with flat MnTe samples[13,14] of 1-mm thickness with lateral dimensions ranging between 4 and 6 mm. The samples were indium bonded to a sapphire delay rod (length: 15 mm, diameter: 10 mm), using the thermocompression method in vacuum. X-cut quartz transducers with fundamental resonance frequencies of 9 and 10 MHz were used to generate and detect longitudinal ultrasonic waves with frequencies up to 530 MHz, operating in overtones. rf pulses with 1-μsec length were applied. Since the ultrasonic attenuation due to lattice imperfections, etc., in MnTe is very high, the influence of multiple reflections inside the MnTe sample on the transmitted-signal amplitude can be neglected. For the same reason the absolute value of ultrasonic attenuation cannot be measured di-

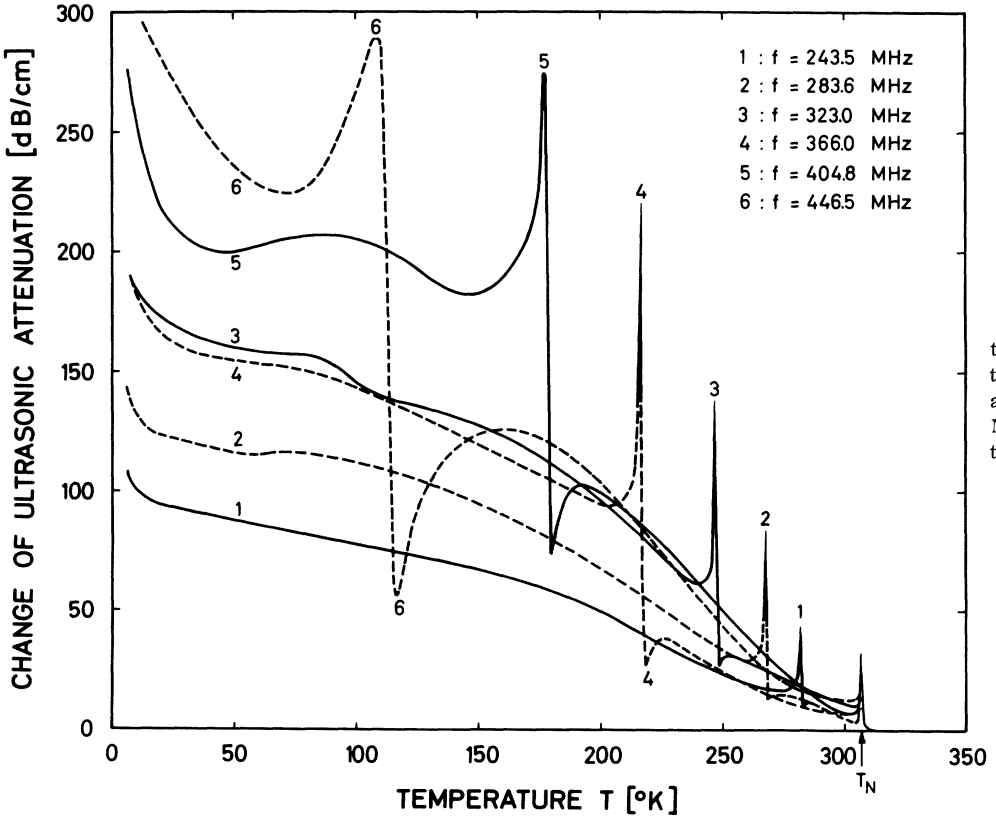

FIG. 1. Temperature dependence of ultrasonic attenuation for a longitudinal wave in MnTe at $H=0$ ($f=243.5$ to 446.5 MHz).

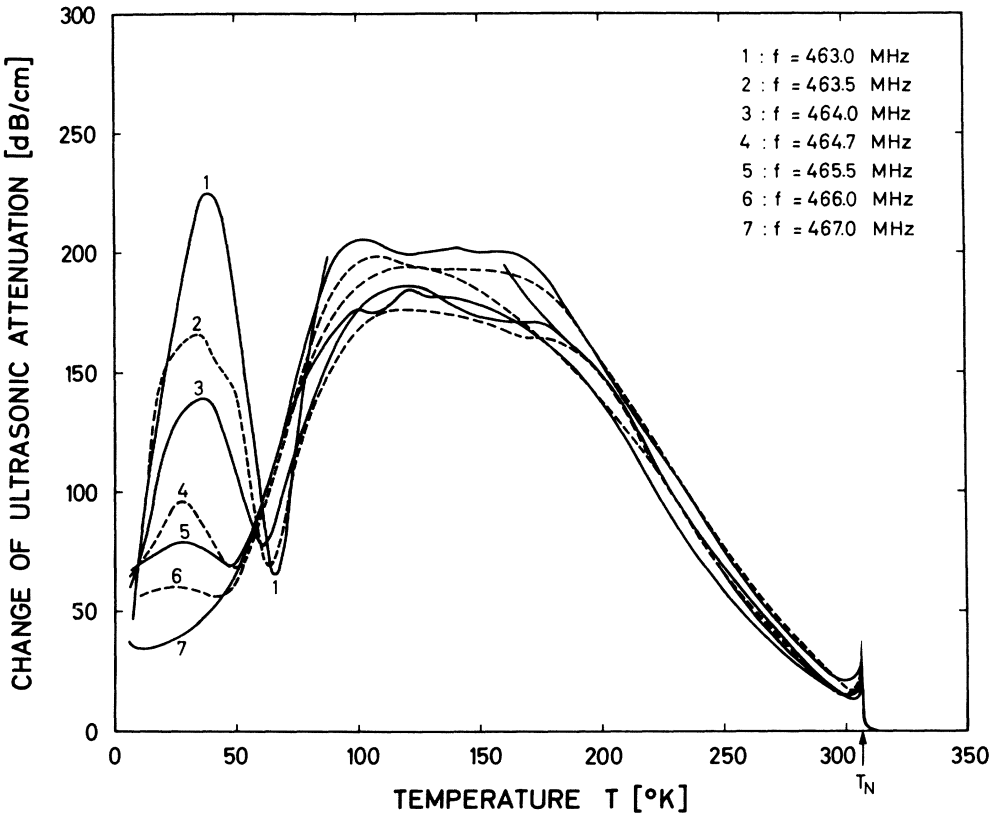

FIG. 2. Temperature dependence of ultrasonic attenuation for longitudinal wave in MnTe at $H = 0$ (f = 463.0 to 467.0 MHz).

rectly. Therefore we quote the changes of the attenuation referred to its value above the Néel temperature, which is fairly constant. The transmitted signal is time selected, and its amplitude is recorded on a logarithmic scale. The sample with the delay rod was mounted with good thermal contact inside a copper block. The temperature was varied either by using a controlled flow of liquid helium around the block or by means of a servo-controlled heater system in thermal contact to a cryogenic reservoir. Temperature was recorded using a chromel-constantan thermocouple for higher temperatures and a carbon resistor below 60 °K.

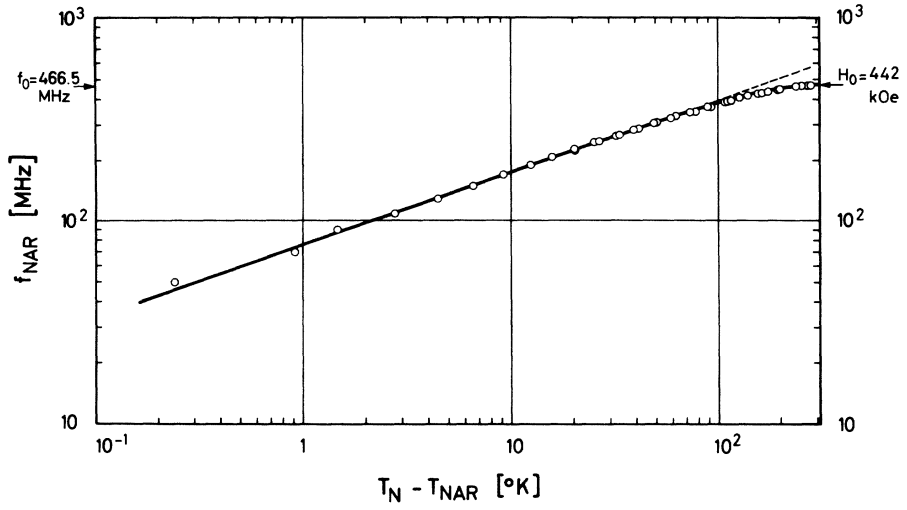

FIG. 3. Temperature dependence of the Mn^{55} NAR frequency in MnTe.

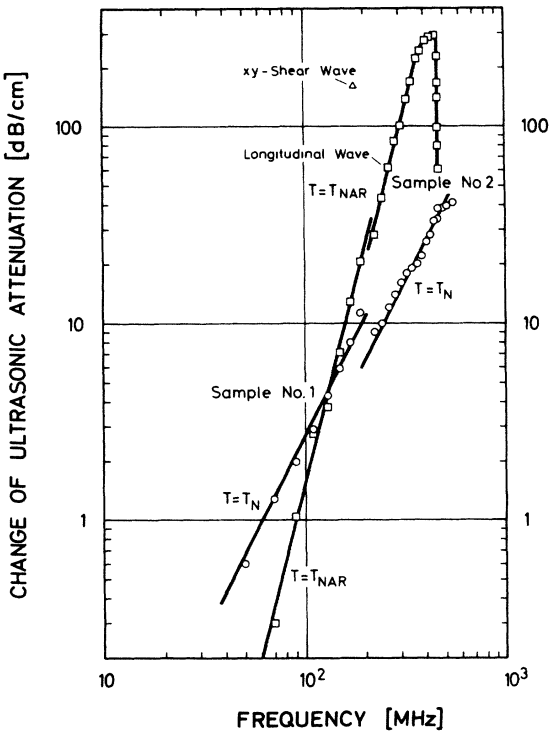

FIG. 4. Frequency dependence of critical attenuation at $T = T_N$ and NAR absorption at $T = T_{NAR}$ for longitudinal waves in MnTe. The triangular point refers to α_{NAR} for the xy shear wave at $f = 178$ MHz.

B. Temperature Dependence of Ultrasonic Attenuation and NAR in MnTe at $H = 0$

The temperature dependence of ultrasonic attenuation for a longitudinal wave in MnTe with a propagation vector in the hexagonal plane is plotted in Figs. 1 and 2 for frequencies between 243.5 and 467 MHz. The narrow absorption peak at the Néel temperature T_N is due to scattering of the phonons by critical magnetic fluctuations, which occur at the antiferromagnetic phase transition. A background absorption, which increases with decreasing temperature, occurs below T_N. The intense frequency-dependent resonance absorption, caused by the Mn^{55} NAR,[3] is superimposed on the background (see Fig. 1). The line shape of the NAR comprises both an absorptive and a dispersive component,[5] which is more pronounced at lower temperatures. The temperature T_{NAR}, at which the NAR absorption occurs, decreases with increasing frequency f. A relation $f_{NAR} \sim (T_N - T_{NAR})^{0.356}$ is satisfied in the temperature range $0.6 \leq T/T_N \leq 1$ (see Fig. 3), which agrees with the expected temperature dependence of the sublattice magnetization $M = M(T)$ in an antiferromagnet[15]: $f_{NAR} = (\gamma_n/2\pi)H_n(T) \sim M(T)$, where γ_n is the nuclear gyromagnetic ratio: $\gamma_n/2\pi = 1.0553$ MHz/kOe for the Mn^{55} nucleus. By extrapolating the NAR frequency to zero temperature, a value $f_0 = 466.5$ MHz is obtained, which corresponds to a hyperfine field of 442 kOe. Results for frequencies below 200 MHz in Fig. 3 were taken from Ref. 3.

Figure 2 shows that the absorptive component of the NAR decreases rapidly for $f > 463$ MHz and completely vanishes for $f > 467$ MHz. For still higher frequencies the attenuation is mainly due to background losses. Frequency pulling effects of the NAR frequencies due to the static nuclear magnetization[16] could not be observed. In all measurements reported, the power level was kept sufficiently low in order to avoid saturation effects of the NAR.

The frequency dependence of critical attenuation at $T = T_N$ and NAR absorption at $T = T_{NAR}$ for longitudinal waves in MnTe is plotted in Fig. 4. Results below $f = 200$ MHz, marked "sample No. 1" were taken from Ref. 3. The critical attenuation at $T = T_N$ increases proportional to ω^2 as predicted by theory.[17] For frequencies up to 400 MHz the peak absorption at the NAR increases proportional to ω^4 with maximum changes of the ultrasonic attenuation up to 300 dB/cm. For the xy shear wave in MnTe no attenuation peak at T_N is observed, and the NAR absorption is approximately ten times as high as compared to the longitudinal wave at the same frequency (see the triangular point at $f = 178$ MHz in Fig. 4). For longitudinal waves propagating along the hexagonal axis no NAR was observed, since no magneto-elastic coupling occurs in this case.

In addition to the peaks in the ultrasonic attenuation at $T = T_N$ and $T = T_{NAR}$ we also observed anomalies in the sound velocity v_s of MnTe at these temperatures. Changes in the sound velocity were measured very accurately using a crystal-controlled oscillator and comparing the phases of the transmitted ultrasonic pulse and the rf drive signal. For different temperatures the frequency of the oscillator was adjusted such as to keep the phase difference between ultrasonic pulse and drive signal constant. Figure 5 shows the resulting frequency change versus temperature for a longitudinal wave transmitted through a system comprising a MnTe sample of thickness 1 mm and a sapphire delay rod of thickness 15 mm. The fractional changes of sound velocity $\Delta v_s/v_s$, given in Fig. 5, refer to the MnTe sample alone and were calculated from the measured change for the whole system, using the thicknesses and sound velocities of sample and delay rod, respectively. For comparison, the change of ultrasonic attenuation at $f = 230$ MHz is plotted in the upper part of Fig. 5. Clearly, the dispersion in the sound velocity coincides with the maximum absorption at $T = T_{NAR}$.

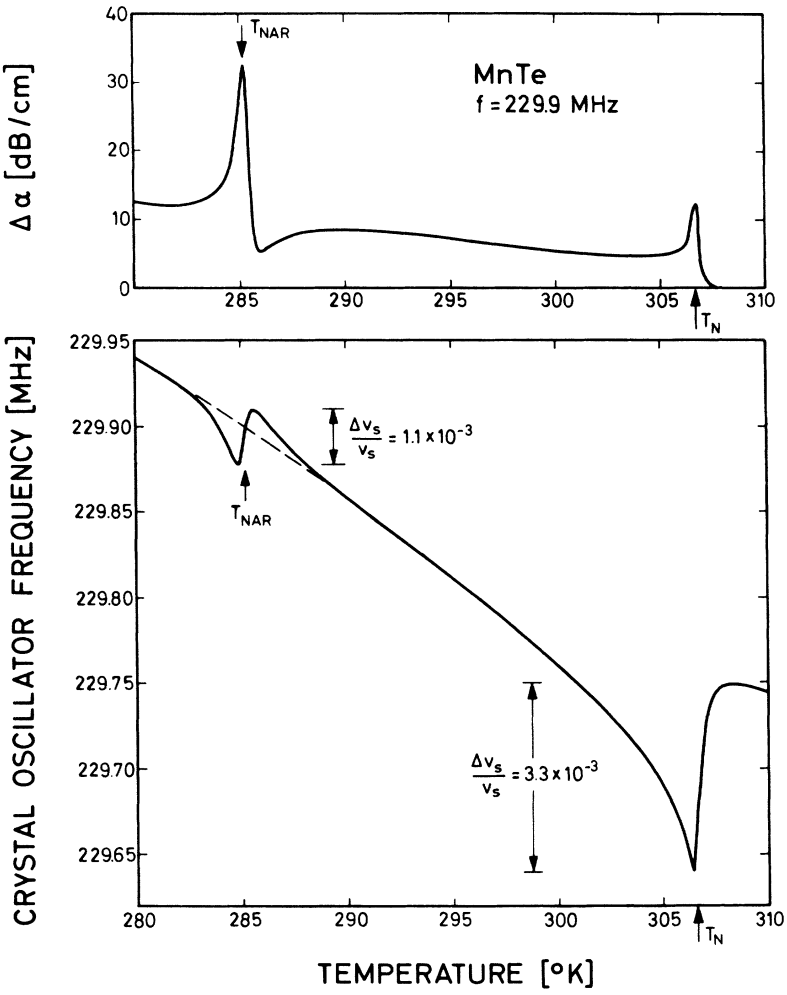

FIG. 5. Change of ultrasonic attenuation at $f = 230$ MHz ($H = 0$) and crystal oscillator frequency (for constant phase superposition) versus temperature for transmission of longitudinal waves through the system: MnTe sample ($d_1 = 1$ mm) + sapphire delay rod ($d_2 = 15$ mm).

C. Magnetic-Field Dependence of Ultrasonic Attenuation and NAR in MnTe

The coordinate system, which is used in order to describe the magnetic-field dependence of background and NAR absorption, is shown in Fig. 6. The x and y axes are, respectively, oriented perpendicular and parallel to one of the Mn-Mn directions in the hexagonal plane. The z direction is chosen parallel to the hexagonal axis. The direction of an external magnetic field H is described by the azimuth angle φ_H. In zero magnetic field the sublattice magnetization may be directed along any one of the "easy" axes $i = 1$, 2, 3, which occur at 60° intervals in the "easy" plane. The location of the easy axes perpendicular to the Mn-Mn directions was determined from measurements of the sixfold component of magnetic torque (Sec. IV).

With a magnetic field applied in the hexagonal plane the ultrasonic attenuation for a longitudinal wave with $q \parallel x$, $f = 276.5$ MHz is shown as a function of temperature in Figs. 7 and 8 for $\varphi_H = 0°$ and 45°, respectively. The observed splitting of the NAR line can be explained by vector addition of the external magnetic field $\vec{H}$ to the hyperfine fields $\vec{H}_n$ corresponding to the antiparallel sublattices of electronic magnetization. For $\varphi_H = 0°$ (Fig. 7) both background and NAR absorptions are reduced drastically in strong fields since in the flopped condition the spins are oriented in a direction, where no magneto-elastic coupling occurs, as will be discussed in Sec. III C. In the case $\varphi_H = 45°$ (see Fig. 8) the NAR absorption is split into four lines. In high fields a magnetic component of the background absorption is still present, and an unsplit NAR line occurring at a slightly higher temperature than for $H = 0$ is observed. This behavior can be explained as follows: The magnetic field at $\varphi_H = 45°$ rotates the spins into a direction of maximum magneto-elastic coupling (see Sec. III C). The external magnetic field $\vec{H}$ is added perpendicular to the considerably larger hyperfine field $\vec{H}_n$, yielding only a small shift of the NAR.

The temperatures of maximum NAR absorption

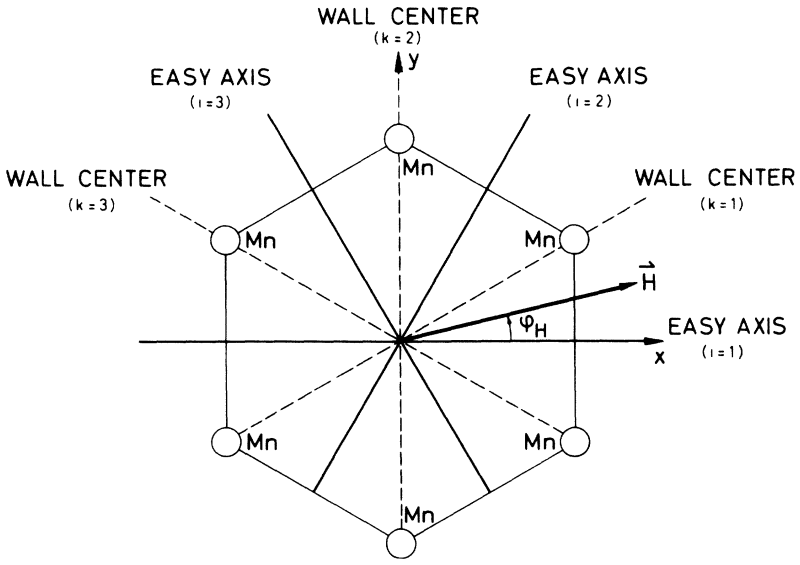

FIG. 6. Coordinate system and location of "easy" axes $i = 1, 2, 3$ and centers $k = 1, 2, 3$ of 60° domain walls within the hexagonal plane of MnTe.

at $f = 276.5$ MHz as a function of magnetic-field orientation in the hexagonal plane are plotted in Fig. 9. The open circles and solid lines correspond to the experimental results, and filled circles and triangles refer to theoretical calculations for domains and domain walls, respectively, and will be discussed in Sec. IV. The appearence of the unsplit center line in the high-field flopped state can be seen clearly for $\varphi_H = 30°$ and 60°, starting at magnetic fields around 6 kOe.

When a magnetic field is applied perpendicular to the hexagonal plane, the NAR line remains unsplit, because $\vec{H} \perp \vec{H}_n$ for all spins in the hexagonal plane, and no spin-flop occurs. Figure 10 shows the temperatures of maximum NAR absorption for the longitudinal wave as a function of magnetic field orientation in the xy, xz, and yz planes. The splitting vanishes when the field direction approaches the hexagonal axis.

III. THEORY

A. Static Equilibrium Conditions for Electronic and Nuclear Spin Systems

The magnetic properties of MnTe are charac-

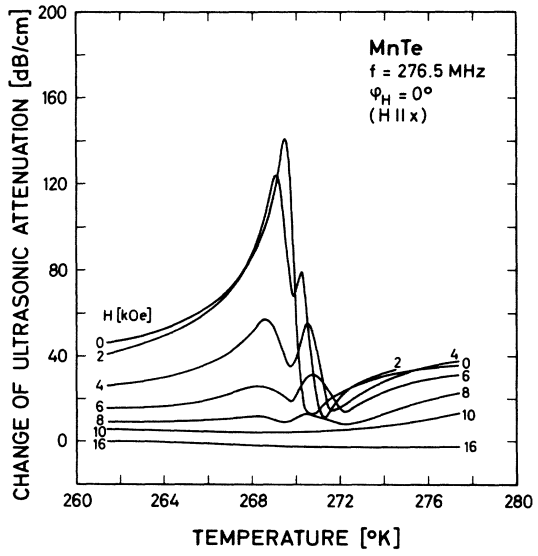

FIG. 7. Temperature dependence of ultrasonic attenuation for a longitudinal wave with $q \parallel x$, $f = 276.5$ MHz in MnTe. Magnetic field H as parameter, $\varphi_H = 0°$.

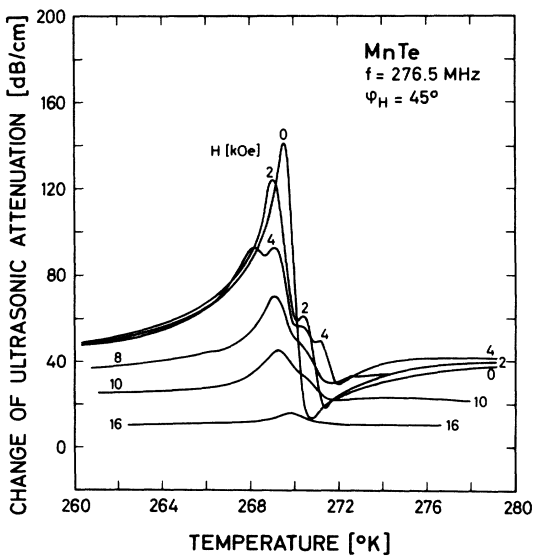

FIG. 8. Temperature dependence of ultrasonic attenuation for a longitudinal wave with $q \parallel x$, $f = 276.5$ MHz in MnTe. Magnetic field H as parameter, $\varphi_H = 45°$.

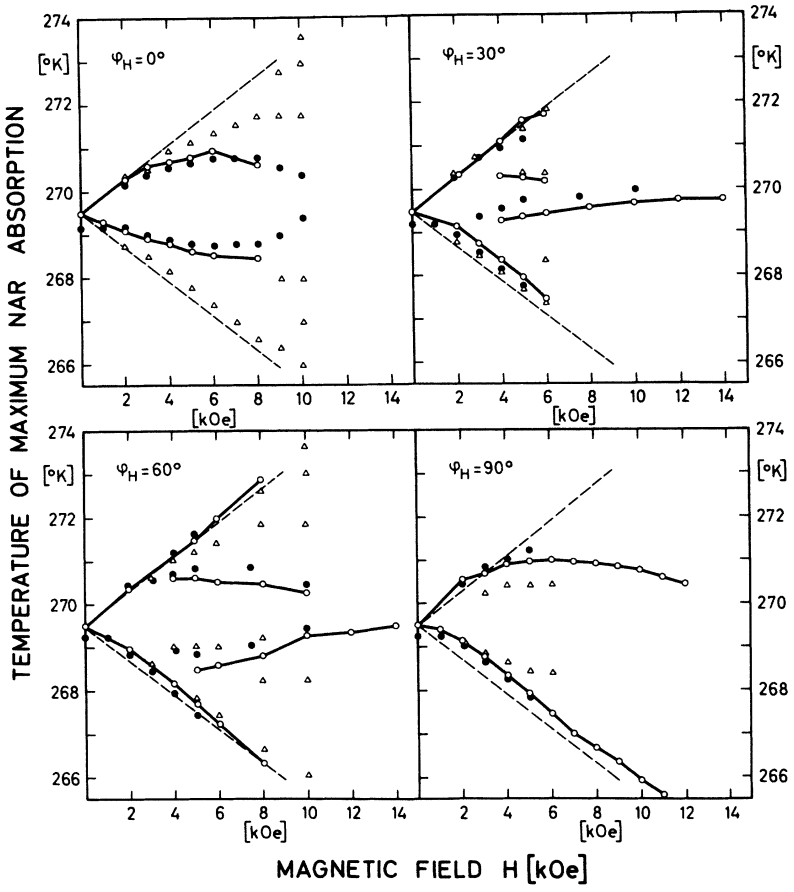

FIG. 9. Temperature of maximum NAR absorption for longitudinal wave with $q \parallel x$, $f = 276.5$ MHz in MnTe as a function of magnetic field for various azimuth angles φ_H. Open circles are experimental points; closed circles are theoretical points for domains [calculated from Eq. (19), using $H_{SF} = 6$ kOe]; open triangles are theoretical points for domain walls [calculated from Eq. (20), using $H_{SF} = 6$ kOe]. The dashed lines correspond to $H_{1,2} = H_n \pm H$.

terized by two sublattices of electronic magnetization $\vec{M}_1$ and $\vec{M}_2$ and two sublattices of nuclear magnetization $\vec{M}_{n1}$, $\vec{M}_{n2}$. A magnetic moment of five Bohr magnetons per Mn atom was determined from susceptibility measurements,[9,10] which agrees with an expected ^6S electronic configuration.[11] The dimensions of the unit cell in the NiAs structure are $a = 4.142$ Å and $c = 6.703$ Å.[6] With two formula units MnTe per cell the calculated density is $\rho = 6.084$ g/cm^3, and the electronic sublattice magnetization at $T = 0\,^\circ$K is $M_0 = 465$ cgs/cm^3.

The static equilibrium positions of the magnetization vectors are described with respect to the (x, y, z) coordinate system of Fig. 6. Let the azimuth angles for the electronic and nuclear sublattice magnetization be φ_1, φ_2, and φ_{n1}, φ_{n2}, respectively. The orientation of the antiferromagnetic vector $\vec{L} = \vec{M}_1 - \vec{M}_2$ as a function of magnetic field is calculated from the following equation[18] neglecting the influence of the static nuclear magnetization[16]:

$$\sin 6\varphi - (H/H_{SF})^2 \sin 2(\varphi - \varphi_H) = 0 , \tag{1}$$

where

$$H_{SF} = [24K_3/(\chi_\perp - \chi_\parallel)]^{1/2} \tag{2}$$

is the spin-flop field, K_3 is the sixfold anisotropy constant, and $\chi_\perp$ and $\chi_\parallel$ are the perpendicular and parallel susceptibilities, respectively. In deriving Eq. (1) the conditions $H^2/H_e^2 \ll 1$ and $(6K_3/M) \ll H_e$ have been used. (H_e = exchange field.) The static equilibrium positions for $H = 0$ are [see Eq. (1)] $\varphi_0 = \frac{1}{3}n\pi$, $n = 0, 1, \ldots, 6$. Under the influence of a magnetic field the $\vec{L}$ vector approaches a position perpendicular to $\vec{H}$ above the spin-flop field. According to Eq. (1) the spin flop occurs at $H = H_{SF}$ for $|\varphi_0 - \varphi_H| = 30^\circ$ and at $H = \sqrt{3}H_{SF}$ for $|\varphi_0 - \varphi_H| = 0^\circ$ or 60°.

For a given orientation of the electronic magnetization the azimuth angles of the nuclear sublattice magnetization can be calculated from an expansion to second order in H/H_n:

$$\cos(\varphi_{n1,2} - \varphi_{1,2}) \simeq 1 - \tfrac{1}{2}(H/H_n)^2 \sin^2(\varphi_{1,2} - \varphi_H) , \tag{3}$$

where $H_n = \alpha M$ is the hyperfine field. The static magnetic fields acting on the nuclear spin systems are

$$H_{1,2} \simeq H_n + H\cos(\varphi_{1,2} - \varphi_H) + \tfrac{1}{2}(H^2/H_n)\sin^2(\varphi_{1,2} - \varphi_H) . \tag{4}$$

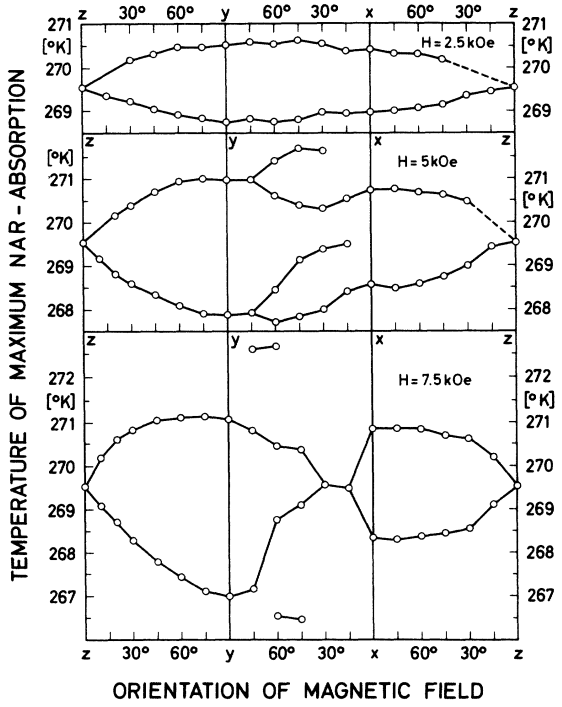

FIG. 10. Temperature of maximum NAR absorption for longitudinal wave with $q \parallel x$, $f = 276.5$ MHz in MnTe as a function of magnetic-field orientation for various values of H.

This equation describes the vector addition of the external magnetic field to the hyperfine field, which determines the splitting of the NAR lines, if frequency pulling effects[16] are neglected at high temperatures.

B. Dynamic Equations for Electronic and Nuclear Spin Systems

The equations of motion for the electronic magnetization are written in the Landau-Lifshitz form:

$$\frac{1}{\gamma_e}\dot{\vec{M}}_{1,2} = (\vec{M}_{1,2}\times\vec{H}^{(e)}_{1,2}) - \frac{\Gamma'}{M}\left[\vec{M}_{1,2}\times(\vec{M}_{1,2}\times\vec{H}^{(e)}_{1,2})\right], \tag{5}$$

with a phenomenological damping parameter Γ'. The effective magnetic fields $H^{(e)}_{1,2}$ acting on the electronic sublattices are calculated from the total magnetic energy density Φ:

$$\vec{H}^{(e)}_{1,2} = -\frac{\partial\Phi}{\partial\vec{M}_{1,2}} \quad . \tag{6}$$

The dynamic equations for the nuclear magnetization are written in the Bloch form:

$$\frac{1}{\gamma_n}\dot{\vec{M}}_{n1,2} = (\vec{M}_{n1,2}\times\vec{H}^{(e)}_{n1,2}) - \overleftrightarrow{\tau}^{-1}\cdot(\vec{M}_{n1,2} - \langle\vec{M}_{n1,2}\rangle), \tag{7}$$

where $\overleftrightarrow{\tau}^{-1}$ is the tensor of reciprocal nuclear relaxation times, and the effective fields acting on the nuclear sublattices are

$$\vec{H}^{(e)}_{n1,2} = \vec{H} + \alpha\vec{M}_{1,2} \quad . \tag{8}$$

The equations of motion are linearized for small-amplitude oscillations using coordinate systems, in which the X axes coincide with the directions of static sublattice magnetization and the Y and Z axes, respectively, refer to oscillations within the hexagonal plane and perpendicular to it. Let the dynamic components of magnetization be $m_Y^{(1,2)}$, $m_Z^{(1,2)}$ for the electronic sublattices and $m_{n,Y}^{(1,2)}$, $m_{n,Z}^{(1,2)}$ for the nuclear sublattices. Then the nuclear variables can be expressed in terms of the dynamic components of electronic magnetization using Eqs. (7) and (8):

$$\begin{pmatrix} m_{n,Y}^{(1,2)} \\ m_{n,Z}^{(1,2)} \end{pmatrix} = \begin{pmatrix} \chi_{YY}^{(1,2)} & \chi_{YZ}^{(1,2)} \\ \chi_{ZY}^{(1,2)} & \chi_{ZZ}^{(1,2)} \end{pmatrix} \begin{pmatrix} m_Y^{(1,2)} \\ m_Z^{(1,2)} \end{pmatrix} \quad . \tag{9}$$

Neglecting frequency pulling,[16] the nuclear resonance functions are given by

$$\begin{aligned}
\chi_{YY}^{(1,2)} &= \chi_T \frac{H_{1,2}^2\cos(\varphi_{1,2}-\varphi_{n1,2})}{H_{1,2}^2-\Omega_n^2}, \\
\chi_{YZ}^{(1,2)} &= -\chi_T \frac{i\Omega_n H_{1,2}}{H_{1,2}^2-\Omega_n^2}, \\
\chi_{ZY}^{(1,2)} &= \chi_T \frac{i\Omega_n H_{1,2}\cos(\varphi_{1,2}-\varphi_{n1,2})}{H_{1,2}^2-\Omega_n^2}, \\
\chi_{ZZ}^{(1,2)} &= \chi_T \frac{H_{1,2}^2}{H_{1,2}^2-\Omega_n^2},
\end{aligned} \tag{10}$$

where $\Omega_n = (1/\gamma_n)(\omega - i/\tau)$, τ is the transverse nuclear relaxation time, $H_{1,2}$ and $\cos(\varphi_{1,2}-\varphi_{n1,2})$ are given by Eqs. (4) and (3). Furthermore we have

$$\chi_T = \frac{\gamma_n}{\gamma_e}\frac{I(I+1)}{3S}\frac{\hbar\omega_n(T=0)}{kT} = \frac{9.84\times10^{-6}}{T(^\circ\mathrm{K})}, \tag{11}$$

where the electronic gyromagnetic ratio is γ_e, I and S are the nuclear and electronic spins, respectively, and k is Boltzmann's constant. The numerical values in Eq. (11) were calculated for Mn^{55} in MnTe: $\gamma_n = 6.6306\times10^3$ sec^{-1}/Oe, $\gamma_e = 1.759\times10^7$ sec^{-1}/Oe, $I = S = \frac{5}{2}$, and $\omega_n(T=0)/2\pi = 466.5$ MHz.

We consider magneto-elastic excitation of the in-plane mode by a small-amplitude ultrasonic wave with strain $e_{ik} = |e_{ik}|e^{i(\omega t-\vec{q}\cdot\vec{r})}$, $\vec{q}$ = wave vector. The dynamic equations for the electronic magnetization can be simplified considerably for frequencies far below the AFMR, i.e., $\omega/\gamma_e \ll (2H_eH_{K_3})^{1/2}$, when the following conditions are satisfied:

$$H_{K_3} \ll H_{K_1}, \quad H^2 \ll 2H_e H_{K_1}, \quad \Gamma'^2 \ll 1, \tag{12}$$

where $H_{K_3} = 36K_3/M$ is the weak in-plane anisotropy field and $H_{K_1} = 2K_1/M$ is the strong out-of-plane anisotropy field. Inserting Eqs. (9) and (10) into (5) and (6) and using the notations

$$m_Y^{\pm} = m_Y^{(1)} \pm m_Y^{(2)}, \qquad m_Z^{\pm} = m_Z^{(1)} \pm m_Z^{(2)}, \tag{13}$$

the dynamic equations for the electronic magnetization can be approximated as

$$\left[H_{K_3}\cos 6\varphi - \frac{H^2}{2H_e}\left(1 - \frac{\chi_\parallel}{\chi_\perp}\right)\cos 2(\varphi - \varphi_H) + \frac{H^2}{2H_e}\frac{\chi_\parallel}{\chi_\perp}\sin^2(\varphi - \varphi_H) - \frac{\Omega^2}{2H_e} + i\Omega\Gamma' + H_n\chi_T - \tfrac{1}{2}H_n(\chi_{YY}^{(1)} + \chi_{YY}^{(2)})\right] m_Y^+ = 2\tau_{Z,me}(\varphi), \tag{14}$$

$$\frac{m_Z^+}{m_Y^+} \approx \frac{i\Omega}{2H_e}, \quad \frac{m_Y^-}{m_Y^+} \approx -\frac{H}{2H_e}\left(1 - \frac{\chi_\parallel}{\chi_\perp}\right)\cos(\varphi - \varphi_H), \quad \frac{m_Z^-}{m_Y^+} \approx \frac{i\Omega H}{H_e H_{K_1}}\left(1 - \frac{1}{2}\frac{\chi_\parallel}{\chi_\perp}\right)\cos(\varphi - \varphi_H), \tag{15}$$

where $\Omega = \omega/\gamma_e$.

The exciting magneto-elastic torque $\tau_{Z,me}$ is calculated from the magneto-elastic energy density[19] neglecting piezomagnetic terms[20] and rotational effects[21,22]:

$$\tau_{Z,me}(\varphi) = MH_{Y,me} = (B_2 - B_1)[(e_{yy} - e_{xx})\sin 2\varphi + e_{xy}\cos 2\varphi]. \tag{16}$$

B_1 and B_2 are magneto-elastic constants.[23] For the frequencies and magnetic fields under consideration, see Eq. (12), the largest dynamic component is m_Y^+. The quantities in Eq. (15) are small, i.e., in this mode the electronic magnetization vectors $\vec{M}_1$ and $\vec{M}_2$ predominantly oscillate antiparallel to each other in the hexagonal plane.

C. Ultrasonic Attenuation and NAR in Domains and Domain Walls

Considering the dominant term in Eq. (14), the dissipated power density for the electronic and nuclear spin systems is

$$P_{\text{diss}} = \tfrac{1}{2}\,\text{Re}\left[i\omega\left(\sum_{j=1}^{2}(\vec{M}_j \cdot \vec{H}_j^{(e)*} + \vec{M}_{nj} \cdot \vec{H}_{nj}^{(e)*})\right)\right] \simeq \tfrac{1}{2}\,\text{Re}(i\omega m_Y^+ H_{Y,me}^*). \tag{17}$$

The sound absorption coefficeint is obtained from

$$\alpha = P_{\text{diss}}/\tfrac{1}{2}\rho v_s^3 |e_{ik}|^2. \tag{18}$$

In the presence of several antiferromagnetic domains $i = 1, 2, 3$ with spin orientations φ_i given by Eq. (1), occupying fractional volumes $V_{d,i}/V$, the ultrasonic attenuation can be calculated from Eqs. (14) and (16)–(18):

$$\alpha_d = \frac{2\omega(B_2 - B_1)^2}{M\rho v_s^3}\sum_{i=1}^{3}\left\{\frac{V_{d,i}}{V}(\Omega\Gamma' - H_n\chi_{n,i}'')\begin{cases}\sin^2 2\varphi_i, & \text{for longitudinal waves}\\ \cos^2 2\varphi_i, & \text{for } xy \text{ shear wave}\end{cases}\right\} \Bigg/ \left\{\left[H_{K_3}\cos 6\varphi_i - \frac{H^2}{2H_e}\left(1 - \frac{\chi_\parallel}{\chi_\perp}\right)\cos^2(\varphi_i - \varphi_H) + \frac{H^2}{2H_e}\frac{\chi_\parallel}{\chi_\perp}\sin^2(\varphi_i - \varphi_H) - \frac{\Omega^2}{2H_e} + H_n\chi_T - H_n\chi_{n,i}'\right]^2 + (\Omega\Gamma' - H_n\chi_{n,i}'')^2\right\}, \tag{19}$$

where

$$\chi_{n,i} = \tfrac{1}{2}[\chi_{YY}^{(1)}(\varphi_i) + \chi_{YY}^{(2)}(\varphi_i)].$$

This equation describes the different loss contributions, which are observed experimentally below T_N (Sec. II): (i) background losses, proportional to Γ', (ii) reactive modulation of the background losses by the nuclei, dispersive component χ_n', and (iii) direct dissipation in the nuclear system, absorptive component χ_n''. The acoustic losses due to electrical conductivity in MnTe[24] are completely negligible in comparison with the magnetic losses, since only the small component m_Z^+ [see Eq. (15)] with net magnetization generates dissipative currents.

In the previous calculations we considered losses due to electronic and nuclear spins, located in domain regions. However, background losses and NAR absorption may also occur due to motion of domain walls.[5,25] In a domain wall the spin orientation $\varphi = \varphi(\xi)$ changes as a function of the coordinate ξ along the wall normal direction. The most important mode of wall motion is the translational mode, for which the influence of the anisotropy field H_{K_3} is compensated by an exchange term,[25]

and a phenomenological wall stiffness field H_K acts as restoring force in the resonance denominator.

We consider domain walls $k=1$, 2, 3 with static spin orientations in the range $\varphi_k^{(1)} \le \varphi_k(\xi) \le \varphi_k^{(2)}$, where the spin directions $\varphi_k^{(1)}$ and $\varphi_k^{(2)}$ in the adjacent domains are calculated from Eq. (1). An approximate calculation of wall absorption yields the following result, assuming $\chi_{\parallel}=0$:

$$\alpha_w \approx \frac{9\omega(B_2-B_1)^2}{\pi M \rho v_s^3} \sum_{k=1}^{3} \left\{ \frac{V_{w,k}}{V} \left(\frac{a_k}{3}\right)^{1/2} \left(\frac{3}{a_k}\Omega\Gamma' - \frac{3}{4}H_n\bar{\chi}''_{n,k}\right) \times \begin{Bmatrix} \langle \sin 2\varphi \rangle^2 \text{ for longitudinal waves} \\ \langle \cos 2\varphi \rangle^2 \text{ for } xy \text{ shear wave} \end{Bmatrix} \Big/ \left[\frac{3}{a_k}\left(H_K - \frac{\Omega^2}{2H_e} + H_n\chi_T\right) - \frac{3}{4}H_n\bar{\chi}'_{n,k}\right]^2 + \left(\frac{3}{a_k}\Omega\Gamma' - \frac{3}{4}H_n\bar{\chi}''_{n,k}\right)^2 \right\}, \tag{20}$$

with $a_k = \pi/(\varphi_k^{(2)} - \varphi_k^{(1)})$, where $V_{w,k}/V$ is the fractional volume occupied by walls of type k. In comparison with Eq. (19) the anisotropy field H_{K_3} in the denominator has been replaced by the wall stiffness field H_K. The numerator of Eq. (20) contains average values of the magneto-elastic torque [see Eq. (16)], describing the strength of excitation of the translational wall mode:

$$\begin{Bmatrix} \langle \sin 2\varphi \rangle \\ \langle \cos 2\varphi \rangle \end{Bmatrix} = \int_{\varphi_k^{(1)}}^{\varphi_k^{(2)}} \begin{Bmatrix} \sin 2\varphi \\ \cos 2\varphi \end{Bmatrix} d\varphi , \quad \begin{matrix} \text{for longitudinal waves} \\ \text{for the } xy \text{ shear wave.} \end{matrix} \tag{21}$$

Weighted average values of the nuclear susceptibilities appear in Eq. (20):

$$\bar{\chi}_{n,k} = \bar{\chi}'_{n,k} + i\bar{\chi}''_{n,k} = \int_{\varphi_k^{(1)}}^{\varphi_k^{(2)}} [\chi_{YY}^{(1)}(\varphi_k) + \chi_{YY}^{(2)}(\varphi_k)] w_k(\varphi)\, d\varphi , \tag{22}$$

where the weighting function

$$w_k(\varphi) = \sin\pi\left(\frac{\varphi_k(\xi) - \varphi_k^{(1)}}{\varphi_k^{(2)} - \varphi_k^{(1)}}\right)$$

reaches a maximum at the wall center and is zero outside the wall. Numerical calculations of the NAR line shape for nuclei in domain walls as a function of an external field yield a split up into several peaks, which are qualitatively similar to those in the case of domain absorption. A distinction between these two cases will be given by a detailed discussion of the experimental results in Sec. IV.

IV. COMPARISON BETWEEN EXPERIMENTAL RESULTS AND THEORY

In order to compare the static equilibrium orientation of the $\vec{L}$ vector with the predictions of Eqs. (1) and (2), measurements of the magnetic torque density τ_H in MnTe were carried out[26] with a field $H=15$ kOe, rotated in the hexagonal plane. Results for the sixfold and twofold torque components as a function of temperature are shown in Fig. 11 (see also Ref. 10). Theory predicts that the sixfold torque component in the high-field flopped condition is field independent[18]:

$$\tau_H = 12K_3 \sin 6\varphi_H . \tag{23}$$

Since the experimental torque curves below $T=260\,^{\circ}$K still increase with H at the highest field available ($H=15$ kOe), values of K_3, calculated from the measured τ_H according to Eq. (23), are too small. The temperature dependence of the sixfold component (Fig. 11) with a maximum around $T=170\,^{\circ}$K cannot yet be interpreted theoretically at the present time. In the range of higher temperatures the anisotropy field $H_{K_3}=36K_3/M$ was calculated, assuming Eq. (23) to be valid and computing $M(T)$ from the temperature dependence of f_{NAR} in Fig. 3, using $M_0=465$ cgs/cm^3. The result is shown as a dotted line in Fig. 11. Using our K_3 values and the published susceptibility data[10] $\chi_{\perp}=1.41\times10^{-4}$ cgs/cm^3 and $\chi_{\parallel}(T)$ we calculate the spin-flop field from Eq. (2): at $T=270\,^{\circ}$K, $K_3\approx1$ erg/cm^3, $1-\chi_{\parallel}/\chi_{\perp}=0.26$, $H_{SF}\approx0.8$ kOe.

This calculated value of the spin-flop field is in striking disagreement with the experimental results for the splitting of the NAR at temperatures around 270 °K (see Fig. 9). A value $H_{SF}\approx0.8$ kOe would imply that all spins are oriented almost perpendicular to H for external fields as low as 1 kOe, i.e., no splitting of the NAR line should be observed. Since the experiments yield values of the spin-flop field around 6 to 10 kOe (see Fig. 9), evidently other contributions, which are presently unknown, in addition to the anisotropy constant K_3, are important in determining the spin orientation. Further investigations are required in order to

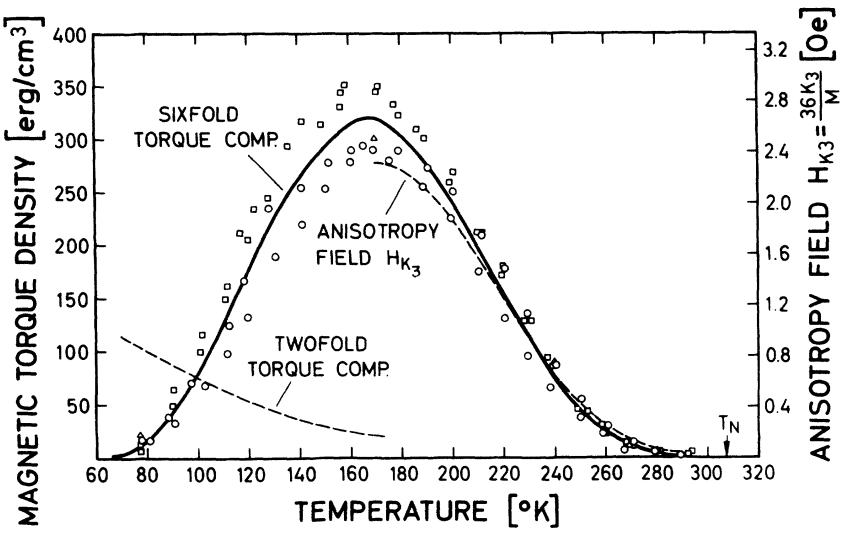

FIG. 11. Magnetic torque density τ_H in MnTe as a function of temperature with $H=15$ kOe rotated in the hexagonal plane. The anisotropy field H_{K_3} was calculated, assuming $\tau_H = 12K_3 \sin 6\varphi_H$ in the flopped state. The experimental points, open circle, open square, and open triangle, refer to different samples.

clarify this point.

Experimental results of ultrasonic background absorption as a function of magnetic field orientation (plotted as solid lines in Figs. 12 and 13) shall be compared with theoretical predictions from Eq. (19). We consider the case $\chi_{\parallel}=0$, neglecting nuclear contributions and assume equal and field-independent domain volumes V_{di}. An expansion of Eq. (19) for small fields $(H/H_{SF})^2 \ll 1$ yields the nonresonant background absorption for the longitudinal wave:

$$\alpha_d = \sum_{i=1}^{3} \alpha_{d,i} \sim \left[1 - \frac{2}{3}\left(\frac{H}{H_{SF}}\right)^2 \cos 2\varphi_H\right] \quad , \qquad (24)$$

which qualitatively agrees with the observed angular dependence of the background absorption for small fields in Fig. 12. However, this agreement has to be considered somewhat fortuitous in view of the severe approximations used in deriving Eq. (24).

In the high-field flopped condition $H^2 \gg H_{SF}^2$, we have for all domains $|\varphi - \varphi_H| = \pi/2$, and the background absorption according to Eq. (19) is

$$\alpha_d \sim \sin^2 2\varphi_H \qquad \text{for longitudinal waves,} \qquad (25)$$

$$\alpha_d \sim \cos^2 2\varphi_H \qquad \text{for the } xy \text{ shear wave ,} \qquad (26)$$

in qualitative agreement with the experimental result in Fig. 13.

Experimental results for the NAR absorption are plotted as open circles in Fig. 13. The angular dependence of α_{NAR} for the longitudinal wave approximately follows a $\sin^2 2\varphi_H$ dependence, and Merry and Bolef[4] obtained an analogous result in $RbMnF_3$. For the xy shear wave, no NAR absorption is observed for $\varphi_H = 45°$, whereas maximum coupling is measured at $\varphi_H = 0°$.

In order to compare the observed NAR splitting (see Fig. 9) with theory, numerical calculations for domain and wall absorption according to Eqs. (19) and (20) were performed, assuming a spin-flop field $H_{SF} = 6$ kOe in the static equilibrium condition [Eq. (1)] in order to obtain rough agreement with the experiments for temperatures around 270 °K. The following numerical parameters were chosen to fit the observed NAR line shape at $H=0$: $H_{K_3} = H_K = 0.7$ Oe, $\Gamma' = 3\times10^{-3}$, $Q_n = \omega\tau = 330$, assuming field-independent domain and wall volumes: $V_{d,1} = V_{d,2} = V_{d,3}$; $V_{w,1} = V_{w,2} = V_{w,3}$. The calculated NAR temperatures as a function of magnetic field for

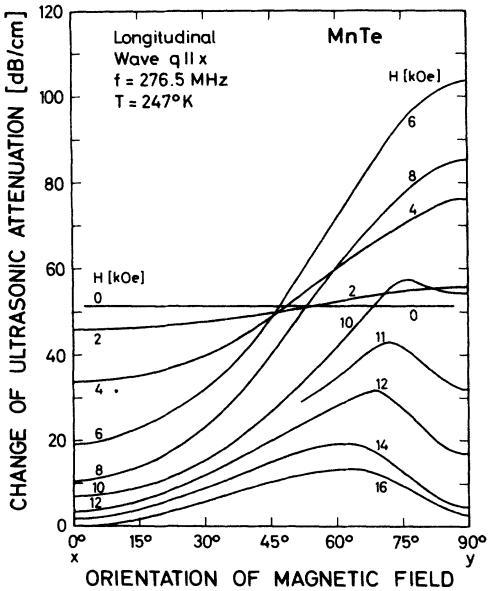

FIG. 12. Background attenuation at $T=247$ °K for longitudinal wave with $q \parallel x$, $f=276.5$ MHz in MnTe as a function of magnetic field orientation φ_H with H as parameter.

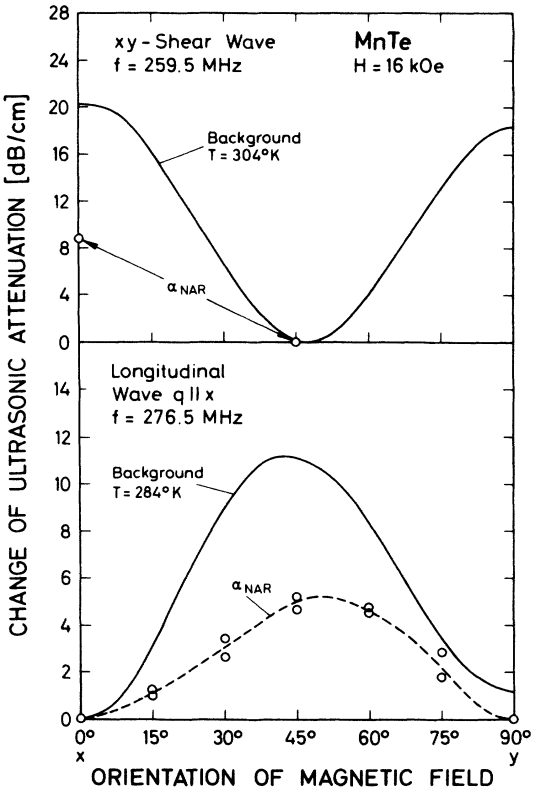

FIG. 13. Measured ultrasonic attenuation at $H = 16$ kOe in MnTe as a function of magnetic field orientation φ_H for the xy shear wave at $f = 259.5$ MHz and the longitudinal wave with $q \| x$ at $f = 276.5$ MHz. Solid line is the background absorption and the open circles represent NAR absorption.

various orientations φ_H are shown in Fig. 9; filled circles and triangles refer to domain and wall absorption, respectively. These results clearly demonstrate that the observed effects are caused mainly by nuclei located within the domains: The measured NAR splitting is larger at $\varphi_H = 90°$ than at $\varphi_H = 0°$, in agreement with theoretical results for domains. An additional reason for excluding an explanation in terms of wall absorption is the observation of the unsplit NAR line for $H \gg H_{SF}$ in Fig. 8. These effects cannot be caused by nuclei located within domain walls, since the coupling factors for wall motion vanish above the spin-flop field [see Eq. (21)]. The dispersive component in the NAR line shape vanishes at higher magnetic fields (see Fig. 8). This observation can be explained by considering the terms proportional to $H^2/2H_e$ in the denominator of Eq. (19), which reduce the reactive modulation of the losses for magnetic fields above the spin-flop field.

In summary, we can state that the observed effects of ultrasonic background and NAR absorption in MnTe for high magnetic fields $H \gg H_{SF}$ agree with theoretical predictions for domain absorption, whereas the behavior for lower fields cannot yet be interpreted quantitatively. In particular, the observed spin-flop fields are much higher than the values calculated from measured susceptiblities and sixfold anisotropy constants.

ACKNOWLEDGMENTS

Fruitful discussions with K. H. Sarges, R. P. van Stapele, D. Polder, B. Schneider, and M. H. Seavey are acknowledged. Special thanks are due to K. H. Sarges for carrying out numerical calculations, to D. Mateika and A. M. J. H. Seuter for supplying MnTe samples. Technical assistance was received from W. Hoppe, D. Restorff, and R. Schulz.

[1]For a review of the NMR in antiferromagnetics see V. Jaccarino, in *Magnetism*, edited by G. Rado and H. Suhl (Academic, New York, 1965), Vol. 2A, Chap. 5.

[2]For a review of the NAR see D. I. Bolef, in *Physical Acoustics*, edited by W. P. Mason (Academic, New York, 1966), Vol. IV, Pt. A, p. 113, Subsequent theoretical work on NAR includes papers by P. A. Fedders, Phys. Rev. B 1, 3756 (1970), and by K. N. Shrivastava and K. W. H. Stevens, J. Phys. C 3, 64(L) (1970).

[3]K. Walther, Solid State Commun. 5, 399 (1967); Phys. Letters 32A, 201 (1970).

[4]Subsequently measurements of the Mn^{55} NAR in $RbMnF_3$ were reported by J. B. Merry and D. I. Bolef, Phys. Rev. Letters 23, 126 (1969), by A. Platzker and F. R. Morgenthaler, Phys. Letters 30A, 515 (1969), and by J. B. Merry and D. I. Bolef, Phys. Rev. B 4, 1572 (1971).

[5]A. C. Gossard and A. M. Portis, Phys. Rev. Letters 3, 164 (1959); A. M. Portis and A. C. Gossard, J. Appl. Phys. 31, 205S (1960).

[6]S. Greenwald, Acta Cryst. 6, 396 (1953).

[7]K. K. Kelley, J. Am. Chem. Soc. 61, 203 (1939).

[8]K. Ozawa, S. Anzai, and Y. Hamaguchi, Phys. Letters 20, 132 (1966).

[9]E. Uchida, H. Kondho, and N. Fukuoka, J. Phys. Soc. Japan 11, 27 (1956).

[10]T. Komatsubara, M. Murakami, and E. Hirahara, J. Phys. Soc. Japan 18, 356 (1963).

[11]N. Kunitomi, Y. Hamaguchi, and S. Anzai, J. Phys. Radium 25, 568 (1964).

[12]N. N. Sirota and G. J. Makovetski, Dokl. Akad. Nauk SSSR 170, 1300 (1966) [Sov. Phys. Doklady 11, 888 (1967)].

[13]Measurements reported in Sec. II B were carried out with MnTe crystals kindly supplied by A. M. J. H. Seuter of Philips Research Laboratories, Eindhoven, The Netherlands.

[14]The MnTe crystals used in the measurements of Sec. II C were grown by D. Mateika of this laboratory by means of a newly developed method: D. Mateika, J. Cryst. Growth (to be published).

[15]J. J. van Loef, Solid State Commun. 4, 625 (1966).

[16]P. G. de Gennes, P. A. Pincus, F. Hartmann-Boutron, and J. M. Winter, Phys. Rev. 129, 1105 (1963).
[17]K. Tani and H. Mori, Phys. Letters 19, 627 (1966).
[18]K. Lee, A. M. Portis, and G. L. Witt, Phys. Rev. 132, 144 (1963).
[19]E. A. Turov and V. G. Shavrov, Fiz. Tverd. Tela 7, 217 (1965) [Sov. Phys. Solid State 7, 166 (1965)].
[20]A. I. Mitsek and V. G. Shavrov, Fiz. Tverd. Tela 6, 210 (1964) [Sov. Phys. Solid State 6, 167 (1964)].
[21]D. E. Eastman, Phys. Rev. 156, 645 (1967).
[22]R. I. Melcher, Phys. Rev. Letters 25, 1201 (1970).
[23]K. Walther and K. H. Sarges, Phys. Letters 36A, 309 (1971).
[24]J. D. Wasscher, Philips Res. Rept. Suppl. No. 8 (1969).
[25]J. M. Winter, Phys. Rev. 124, 452 (1961).
[26]The experiments were performed by J. Hewett of Mullard Research Laboratories, Redhill, Surrey, England.

PHYSICAL REVIEW B VOLUME 4, NUMBER 11 1 DECEMBER 1971

Imprisonment of Resonance Radiation in Solids and Gases

Charles W. Scherr
Department of Physics, The University of Texas, Austin, Texas 78712
(Received 20 July 1971)

The description of the self-imprisonment of resonance radiation in gases or solids and of the density distribution of excited species depends upon a transmission coefficient $T(\rho)$, the probability that a quantum of emitted radiation will traverse a thickness ρ of material. This coefficient is shown to be given by the rapidly convergent series $T(\rho)=\sum_n(-k_0\rho)^n/n!(n+1)^{1/2}$, where k_0 is a constant characteristic of the excited species and of the temperature. The above expression is used to give the first accurate discussion of resonance radiation confined between infinite parallel planes, and of radiation inside a sphere over a wide range of $k_0\rho$ values.

I. INTRODUCTION

Resonance radiation is emitted by an excited atom when it makes a transition directly to its ground state. Such radiation is strongly absorbed by other atoms of the same kind when in their normal states. The absorbing atoms are raised to the same state of excitation as the original atom, and can in turn emit the same quantum of energy in order to return to their ground state. Thus, in a volume of gas, the same quantum of energy may be absorbed and reemitted many times over before it reaches the walls of the container. Under these conditions, the radiation is said to be imprisoned.

In a paper[1] bearing nearly the same title as the present one, Holstein has discussed the imprisonment of resonance radiation in terms of a probability $T(\rho)$ that a quantum of emitted radiation passes through a thickness ρ of gas. In Holstein's basic equation[2] for $T(\rho)$, the absorption coefficient of the gas, $k(\nu)$, is explicitly considered as a function of the frequency, so that an averaging of the monochromatic transmission factor, $e^{-k(\nu)\rho}$, over the entire frequency spectrum $P(\nu)$ of the emitted radiation at a given point must be taken. Then

$$T(\rho)=\int P(\nu)e^{-k(\nu)\rho}d\nu\ . \tag{1.1}$$

Of the various forms that the frequency variation can assume, this paper will concern itself only with the Doppler-broadened absorption. In the notation employed by Holstein, $k(\nu)$ is given for Maxwellian velocity distributions by

$$k(\nu)=k_0\exp\{-[(\nu-\nu_0)/\nu_0]^2(c/v_0)^2\}\ , \tag{1.2}$$

where $v_0^2=2RT/M$, and k_0 depends on v_0 and on known spectral characteristics of the normal and excited atomic states. It can be shown[1] that

$$pP(\nu)=k(\nu) \tag{1.3}$$

may be used when the shape of the resonance line is Gaussian, as is the case with Doppler broadening or for the luminescence of certain solids emitting at low temperatures. The proportionality constant p is determined by the requirement

$$\int P(\nu)\,d\nu=1\ . \tag{1.4}$$

Let

$$x=[(\nu-\nu_0)/\nu_0](c/v_0)\ . \tag{1.5}$$

Then it will follow that

$$k(x)=pP(\nu)=k_0e^{-x^2}\ , \tag{1.6}$$

with

$$p=\pi^{1/2}k_0\ , \tag{1.7}$$

whence

$$T(\rho)=\pi^{-1/2}\int_{-\infty}^{\infty}e^{-x^2}e^{-k_0\rho e^{-x^2}}dx\ . \tag{1.8}$$

The further transformation